AGU PUBLICATIONS

JGR

Journal of Geophysical Research: Atmospheres

RESEARCH ARTICLE

10.1002/2013JD020931

Key Points:
- Convective overshooting and transport are sensitive to stratospheric stability
- ARW-WRF model is capable of simulating representative convective depths
- Choice of model microphysics scheme has negligible impact

Correspondence to:
C. R. Homeyer,
chomeyer@ucar.edu

Citation:
Homeyer, C. R., L. L. Pan, and M. C. Barth (2014), Transport from convective overshooting of the extratropical tropopause and the role of large-scale lower stratosphere stability, *J. Geophys. Res. Atmos.*, *119*, 2220–2240, doi:10.1002/2013JD020931.

Received 24 SEP 2013
Accepted 21 FEB 2014
Accepted article online 24 FEB 2014
Published online 12 MAR 2014

Transport from convective overshooting of the extratropical tropopause and the role of large-scale lower stratosphere stability

Cameron R. Homeyer[1], Laura L. Pan[1], and Mary C. Barth[1]

[1] National Center for Atmospheric Research, Boulder, Colorado, USA

Abstract Simulations of observed convective systems with the Advanced Research Weather Research and Forecasting (ARW-WRF) model are used to test the influence of the large-scale lower stratosphere stability environment on the vertical extent of convective overshooting and transport above the extratropical tropopause. Three unique environments are identified (double tropopause, stratospheric intrusion, and single tropopause), and representative cases with comparable magnitudes of convective available potential energy are selected for simulation. Convective injection into the extratropical lower stratosphere is found to be deepest for the double-tropopause case (up to 4 km above the lapse-rate tropopause) and at comparable altitudes for the remaining cases (up to 2 km above the lapse-rate tropopause). All simulations show evidence of gravity wave breaking near the overshooting convective top, consistent with the identification of its role as a transport mechanism in previous studies. Simulations for the double-tropopause case, however, also show evidence of direct mixing of the overshooting top into the lower stratosphere, which is responsible for the highest levels of injection in that case. In addition, the choice of bulk microphysical parameterization for ARW-WRF simulations is found to have little impact on the transport characteristics for each case.

1. Introduction

Stratosphere-troposphere exchange (STE) changes the concentration and distribution of important greenhouse gases in the upper troposphere and lower stratosphere (UTLS) and has been shown to have significant impacts on chemistry, climate, and the radiation budget [e.g., *Holton et al.*, 1995; *Stohl et al.*, 2003]. Most studies of STE focus on important large (planetary and synoptic) scale processes such as the Brewer-Dobson circulation, Rossby wave breaking, and tropopause folding (or stratospheric intrusions), for which broad aspects of the dynamics and chemistry are well known. Despite an extensive understanding of large-scale processes, the role of transport at smaller scales (mesoscale or microscale) such as that in deep tropopause-penetrating convection has not been well examined and is not resolved in current global climate models. In particular, convective transport occurs globally and has the ability to rapidly inject water vapor and additional short-lived tropospheric boundary layer species into the dry lower stratosphere. However, the frequency, vertical extent, irreversibility, and sensitivity to the background meteorological state for convective overshooting events are not well understood. In the tropics, deep convection is considered to play a significant role in water vapor transport into the stratosphere, but whether the process dehydrates or hydrates the tropical tropopause layer (TTL) is a topic of ongoing research [e.g., *Sherwood and Dessler*, 2000; *Jensen et al.*, 2007; *Corti et al.*, 2008; *Hassim and Lane*, 2010]. In the midlatitudes, convective transport may also play an important role in determining the water vapor variability in the extratropical lower stratosphere, which has recently been shown to significantly impact the rate of global climate change [e.g., *Solomon et al.*, 2010]. In addition, *Anderson et al.* [2012] have recently suggested the possibility of chlorine activation and associated ozone destruction from deep injection of water vapor into the extratropical lower stratosphere, which could lead to significant impacts in the radiation budget and human exposure to UV radiation at the surface if convective intensity and frequency were to increase in a warming climate. Understanding and quantifying the impact of convective transport is a critical step for predicting chemistry-climate interactions.

There have been numerous observational studies that show direct and indirect evidence of STE in extratropical convection [e.g., *Poulida et al.*, 1996; *Fischer et al.*, 2003; *Fromm and Servranckx*, 2003; *Dessler and Sherwood*, 2004; *Hegglin et al.*, 2004; *Ray et al.*, 2004; *Hanisco et al.*, 2007; *Anderson et al.*, 2012]. The majority

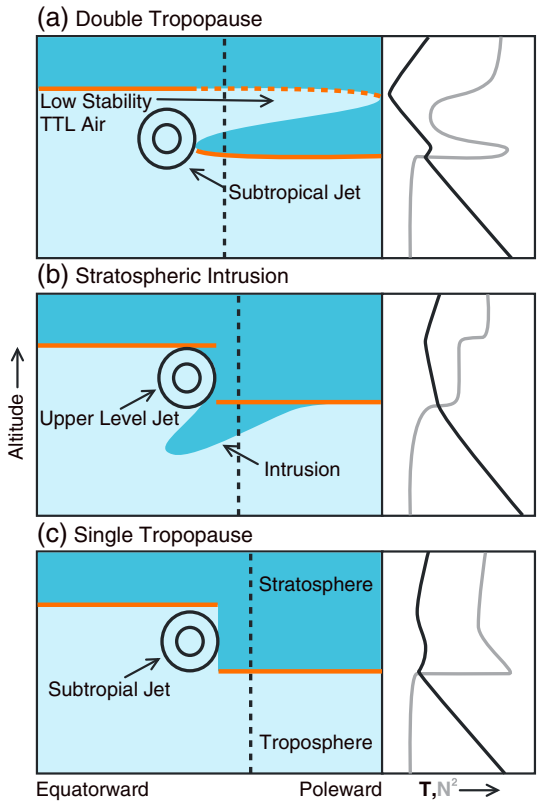

Figure 1. Illustrations of the three background states tested in this study: (a) double tropopause, (b) stratospheric intrusion, and (c) single tropopause. (left) The dashed black lines in the vertical sections identify the locations of (right) the profiles of temperature (T, black) and static stability (Brunt-Väisälä frequency squared, N^2, gray), and the solid and dashed orange lines in each vertical section show the primary and secondary lapse-rate tropopauses, respectively.

of these studies focus on convective injection of water vapor and additional tropospheric trace gases into the extratropical lower stratosphere and often show that convective transport and mixing can be confined to distinct and shallow vertical layers. In addition, most observational studies of STE in convection involve aircraft measurements, since measurements from other platforms (e.g., satellite, radar, and sounding data) are often limited in space and/or time and are not capable of detecting transport and mixing at sufficiently small spatial scales. Recent advances in computational efficiency and numerical modeling, however, have enabled explicit simulation of convection and associated transport in the extratropical UTLS, which is a topic of research that has received increasing attention [e.g., *Gray*, 2003; *Wang*, 2003; *Mullendore et al.*, 2005; *Lane and Sharman*, 2006; *Chagnon and Gray*, 2007; *Luderer et al.*, 2007; *Chagnon and Gray*, 2010; *Tang et al.*, 2011; *Le and Gallus*, 2012]. One of the main findings from these numerical simulations is the critical role of gravity wave breaking in facilitating irreversible transport in overshooting convection. This prevalence of gravity wave breaking has also been observed in modeling studies of overshooting convection in the tropics and is shown to produce significant moistening of the lower stratosphere [e.g., *Hassim and Lane*, 2010]. In addition to wave breaking, some simulations show that direct mixing of the overshooting convective top into the lower stratosphere is also possible [e.g., *Wang*, 2003]. Further studies of simulated convection are required to examine the sensitivity of transport to model parameterizations, resolution, and initialization. Additional measurements of overshooting convection are also required to examine the frequency and extent of STE and to validate the model results.

As previously outlined, one unknown factor in the occurrence and extent of overshooting extratropical convection and transport is the role of the large-scale environment. *Lane and Sharman* [2008] have illustrated the importance of lower stratosphere wind shear and stability in controlling the intensity and extent of gravity wave activity (and related mixing) above overshooting convective clouds. In particular, the turbulent intensity (mixing) and extent are directly related to the magnitude of lower stratosphere wind shear. The lower stratosphere stability, however, is shown to play a less important role and affects primarily the extent of wave activity, which decreases as the stability increases. More recently, aircraft observations of convective injection of water vapor into the lower stratosphere have shown that the depth of overshooting may be largely determined by the stability of the lower stratosphere and that exceptionally deep overshooting (up to 5 km above the lapse-rate tropopause) can be observed within regions of double tropopauses (C. R. Homeyer et al., in preparation, 2013). An illustration of this large-scale environment is given in Figure 1a. Figure 1a (left) shows a vertical cross section of the troposphere and lower stratosphere with an upper tropospheric jet and tropopause heights superimposed, and Figure 1a (right) shows characteristic temperature and static stability profiles on the extratropical (poleward) side of the jet. Large-scale double-tropopause environments are primarily sourced by poleward transport of TTL air into the extratropical lower stratosphere at altitudes above the subtropical jet during Rossby wave-breaking events. This extension of cold TTL air north of the subtropical jet introduces large decreases in static stability in the extratropical lower stratosphere for several kilometers above the primary tropopause, and identification of the chemical

characteristics of these large-scale transport events has received recent attention [e.g., *Pan et al.*, 2009; *Homeyer et al.*, 2011].

An additional unique stability transition in the UTLS is associated with deep descent of lower stratosphere air into the troposphere on the cyclonic side of an upper troposphere jet (a stratospheric intrusion or tropopause fold), for which cyclonic stretching of the atmospheric column decreases the stability of the lower stratosphere and broadens the otherwise sharp transition in stability at the tropopause [e.g., *Reed*, 1955; *Keyser and Shapiro*, 1986]. This large-scale stability environment has been a focus of previous studies that evaluate stratosphere-to-troposphere transport in extratropical convection [e.g., *Gray*, 2003; *Chagnon and Gray*, 2007, 2010]. An illustration of the large-scale environment during a stratospheric intrusion event is given in Figure 1b. Although significant, the magnitude of the reduction in stability in the lower stratosphere for a stratospheric intrusion is often less than that for the double-tropopause environment.

In the absence of unique stability environments introduced by the large-scale dynamical processes of double tropopauses and stratospheric intrusions, the extratropical UTLS often resembles characteristics representative of the climatological mean state. This large-scale environment is referred to here as a "single-tropopause" case (Figure 1c) and is consistent with recent studies of high-resolution radiosonde data in the extratropical UTLS. In particular, profiles for single-tropopause events are characterized by a sharp, shallow temperature inversion above the tropopause that is associated with a large peak in static stability (a tropopause inversion layer (TIL) [e.g., *Birner et al.*, 2002; *Birner*, 2006]). The stability in the lower stratosphere above the TIL reduces slightly but remains significantly higher than that for double-tropopause and stratospheric intrusion environments.

In this study, the influence of the large-scale UTLS environment on the extent of troposphere-to-stratosphere transport in extratropical convection is examined using explicit simulations of observed overshooting convection events at high horizontal and vertical resolution for each of the three large-scale stability environments outlined above: double tropopause, stratospheric intrusion, and single tropopause. In the remaining sections, an outline of the model used and cases chosen for simulations of overshooting convection are presented. Because there are significant differences in the size and lifetime of convective events between the three analyzed case studies, quantitative transport estimates are not discussed. Any transport characterizations presented are qualitative and represent the fraction of the local stratosphere that is influenced by convective injection rather than the mass flux across the tropopause.

2. Model Description and Methods

For simulations of convective overshooting, version 3.4.1 of the Advanced Research Weather Research and Forecasting (ARW-WRF) model is used [*Skamarock et al.*, 2008]. ARW-WRF is a fully compressible, nonhydrostatic three-dimensional cloud resolving model that is commonly used for mesoscale weather prediction. ARW-WRF simulations with two-way nesting are performed, where a coarse outer domain provides boundary values for the finer nested domain and the nested domain returns its calculation back to the outer domain. Figure 2a shows the outer (d01) and nested (d02) domains for each of the three large-scale stability cases. In each simulation, the horizontal resolution of the outer domain is 15 km and the resolution of the nested domain is 3 km. Figure 2b shows the vertical resolution used for all domains, which is highest in the boundary layer and UTLS ($\leq$200 m) and reduced in the middle troposphere and stratospheric "overworld" (altitudes above 380 K potential temperature). For the three large-scale environments outlined in section 1, real cases with comparable magnitudes of convective available potential energy (CAPE) were identified using large-scale analyses, radiosonde data, and radar observations over the continental United States. Although not shown, the CAPE for each case is near 1500 J kg^{-1} and the lower stratosphere wind shear (up to 4 km above the tropopause) is 2–4 m s^{-1} km^{-1} (small compared to the range tested in *Lane and Sharman* [2008]). The duration of each model simulation is 24 h, initialized at 12 UTC on 8 April 2011 for the double-tropopause case, 12 UTC on 21 May 2011 for the stratospheric intrusion case, and 12 UTC on 18 June 2011 for the single-tropopause case and retained for analysis at 1 h intervals.

It is important to note that there are some limitations for simulations with explicitly resolved convection at horizontal grid spacing of *O*(1 km) that may directly impact transport and STE. In particular, simulations at *O*(1 km) grid spacing have been shown to overpredict the horizontal scales of convective updrafts and underpredict gravity wave and turbulence spectra generated by convection [e.g., *Bryan et al.*, 2003; *Lane and Knievel*, 2005; *Bryan and Morrison*, 2012]. However, the vertical velocity within simulated storms has been

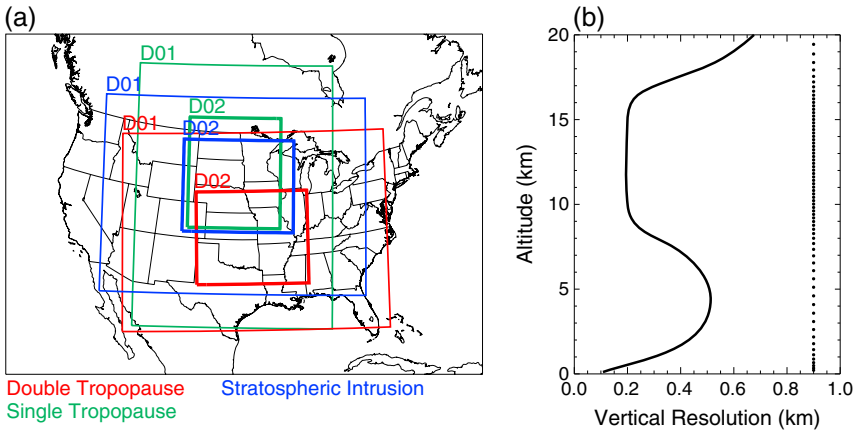

Figure 2. For ARW-WRF simulations, (a) outer (D01) and nested (D02) domains for the double-tropopause case (red), stratospheric intrusion case (blue), and single-tropopause case (green), and (b) model vertical resolution as a function of altitude. Black dots in Figure 2b show altitudes of the individual model levels.

shown to rapidly increase with decreasing grid spacing due to changes in nonhydrostatic pressure perturbation, which may partially compensate for decreases in convective updraft scales [e.g., *Weisman et al.*, 1997; *Cotton et al.*, 2011]. Although changes in quantitative transport estimates are likely for changes in the model resolution, it is not known if changes in the qualitative aspects of transport (the focus of this study) are significant. The results from *Bryan and Morrison* [2012] do show for an idealized case that although the quantitative estimates of transport change when the horizontal grid spacing is decreased, the qualitative aspects of transport are largely independent of model grid spacing, which provides increased confidence in the results presented in this study.

In order to ensure that the full three-dimensional extent of overshooting storms and associated transport are captured in the ARW-WRF simulations, a model top of 10 hPa (~30 km) is used. In addition, because ARW-WRF provides extensive options for the parameterization of cloud microphysics, moist convection, the planetary boundary layer (PBL), and other physical processes and the goal of this study is to identify qualitative aspects of cross-tropopause convective transport, only the cloud microphysics parameterization is varied for simplicity. The PBL parameterization used for all domains and simulations is the Yonsei University scheme [*Hong et al.*, 2006]. Because the grid spacing of the nested domains is not sufficiently small in the horizontal, subgrid scale mixing in each simulation is accomplished in the vertical by the PBL parameterization, while the Smagorinsky first-order closure is used in the horizontal. Potential differences in transport for simulations where the vertical mixing is determined from three-dimensional turbulence closure, which typically requires horizontal grid spacing less than 2 km, are not known. For moist convection, the modified Tiedtke parameterization is used in the outer 15 km domain [*Tiedtke*, 1989; *Zhang et al.*, 2011], while convection is explicitly resolved in the nested 3 km domains.

The choice to vary only the bulk microphysics parameterization (BMP) in this study is motivated primarily by the goal of providing insights into qualitative differences in transport between the three large-scale stability environments. Although variations in additional physical processes such as the PBL parameterization are expected to affect convective initiation, quantitative transport estimates, and the identified source air mass (PBL, middle troposphere, etc.), extensive testing with the ARW-WRF model suggests that varying only the PBL parameterization has little impact on the vertical extent of simulated convection (C. Stephan, personal communication, 2013). In comparison, the choice of BMP can have a large impact on the physical and dynamical nature of simulated convection and its vertical extent [e.g., *Morrison and Milbrandt*, 2011]. As a result, an important goal of this study is to examine the fidelity of two classes of BMPs for providing representative depths of tropopause-penetrating convection, which directly impacts the qualitative aspects of transport above the tropopause. Two BMPs that explicitly predict cloud water, rain, cloud ice, snow, and graupel are tested with the ARW-WRF model: Thompson [*Thompson et al.*, 2008] and Morrison [*Morrison et al.*, 2009]. The Thompson BMP is a single-moment scheme with the exception of cloud ice. The common predicted moment of each hydrometeor is the mass mixing ratio, while the second moment for cloud ice is the number concentration. In addition, the number concentration for rain, graupel, and snow in the Thompson

BMP varies with the mixing ratio. The Morrison BMP is a double-moment scheme that predicts the mixing ratio and number concentration of each hydrometeor. Apart from the differences in the number of moments predicted between the Thompson and Morrison BMPs, the two differ in their treatment of snow. Snow in the Thompson BMP is assumed to be composed primarily of fractal-like aggregates with a density that varies inversely with size, while the Morrison BMP assumes constant-density spherical snow particles.

For model initialization and lateral boundary conditions of the outer 15 km domain, large-scale fields from the ERA-Interim global atmospheric reanalysis produced by the European Center for Medium-Range Weather Forecasts (ECMWF) are used [*Dee et al.*, 2011]. The ERA-Interim fields are available every 6 h on a $0.75° \times \sim 0.75°$ (~80 km) horizontal Gaussian grid and at 37 pressure levels in the vertical from 1000 to 1 hPa. The ERA-Interim is chosen due to the availability of relatively high vertical resolution in the UTLS, which is typically between 500 and 1000 m, while that provided by most large-scale operational analyses in the UTLS is 1000 to 2000 m. In addition, lapse-rate tropopause information in the ERA-Interim and ARW-WRF simulations is determined following the definition of the World Meteorological Organization (WMO): "the lowest altitude at which the temperature lapse rate decreases to 2 K km^{-1}, provided that the average lapse rate between this level and all higher levels within 2 km does not exceed 2 K km^{-1}", where the lapse rate, Γ, is defined as the negative of the vertical temperature gradient ($\Gamma = -\partial T/\partial z$) [*World Meteorological Organization*, 1957]. Additional tropopauses in the WMO definition are defined following the criteria outlined above "if above the first tropopause the average lapse rate between any level and all higher levels within 1 km exceeds 3 K km^{-1}".

Maps of upper tropospheric wind speed and geopotential height and vertical cross sections through the regions of convective development from the ERA-Interim at 18 UTC on the start date for the three select cases are shown in Figure 3. Corresponding temperature and static stability profiles within the regions of convective development and at relative altitude to the primary lapse-rate tropopause are given in Figure 4. In accordance with the WMO definition, green colors in the vertical sections of Figure 3 represent tropospheric values of the vertical temperature lapse rate (i.e., Γ greater than 2 K km^{-1}), and blue colors represent stratospheric values. There is no well-defined subtropical jet for the double-tropopause case (Figure 3a). However, a deep layer of tropospheric temperature lapse rates is observed in the extratropical lower stratosphere well north of the sharp decrease in primary tropopause heights from the tropics (~16 km) to the extratropics (~12 km), producing an extensive double-tropopause feature over the central continental United States. The corresponding profiles in Figure 4 show the large decrease in temperature and static stability from 2 to 5 km above the tropopause associated with this poleward excursion of cold TTL air.

The stratospheric intrusion case (Figure 3b) is associated with a deep midlatitude low-pressure system near the border of Nebraska and South Dakota. In the vertical section, potential vorticity contours on the cyclonic side of the upper tropospheric jet show the descent of the intrusion into the middle troposphere (as low as 6 km), with lapse rates near the 2 K km^{-1} tropopause threshold throughout the depth of the intrusion. The corresponding temperature and stability profiles on the cyclonic side of the jet (blue lines in Figure 4) illustrate the broad transition in stability near the tropopause and the decreased stability of the lower stratosphere compared to the single-tropopause case.

The single-tropopause case (Figure 3c) is also within the Nebraska-South Dakota region, with extratropical tropopause heights near 11 km. Despite the higher vertical resolution of the ERA-Interim, the vertical grid spacing is often too coarse to represent the typically sharp temperature and stability inversion above the extratropical tropopause observed from radiosondes, evident in the green profiles in Figure 4. The stability throughout the lower stratosphere for the single-tropopause environment, however, remains significantly higher than that for the double-tropopause and stratospheric intrusion cases.

For analysis of the vertical extent of simulated storms and comparison with observations, built-in routines in the ARW-WRF model are used to compute the equivalent horizontally polarized radar reflectivity for a 10 cm wavelength (S-band) radar. These routines are based on that outlined in *Morrison et al.* [2009], taking into account Rayleigh scattering only (sufficient for comparisons with S-band radar) and the effects of partially melted graupel and snow. The simulated cloud top, taken as the highest altitude of cloud particle concentrations of 0.1 per liter, is also used to determine the vertical extent of each storm. Observational data used for comparison with the simulated fields are from the Next Generation Weather Radar (NEXRAD) program Weather Surveillance Radar—1988 Doppler (WSR-88D) network in the continental United States [*Crum and Alberty*, 1993]. The WSR-88Ds are S-band radars that are continuously operated

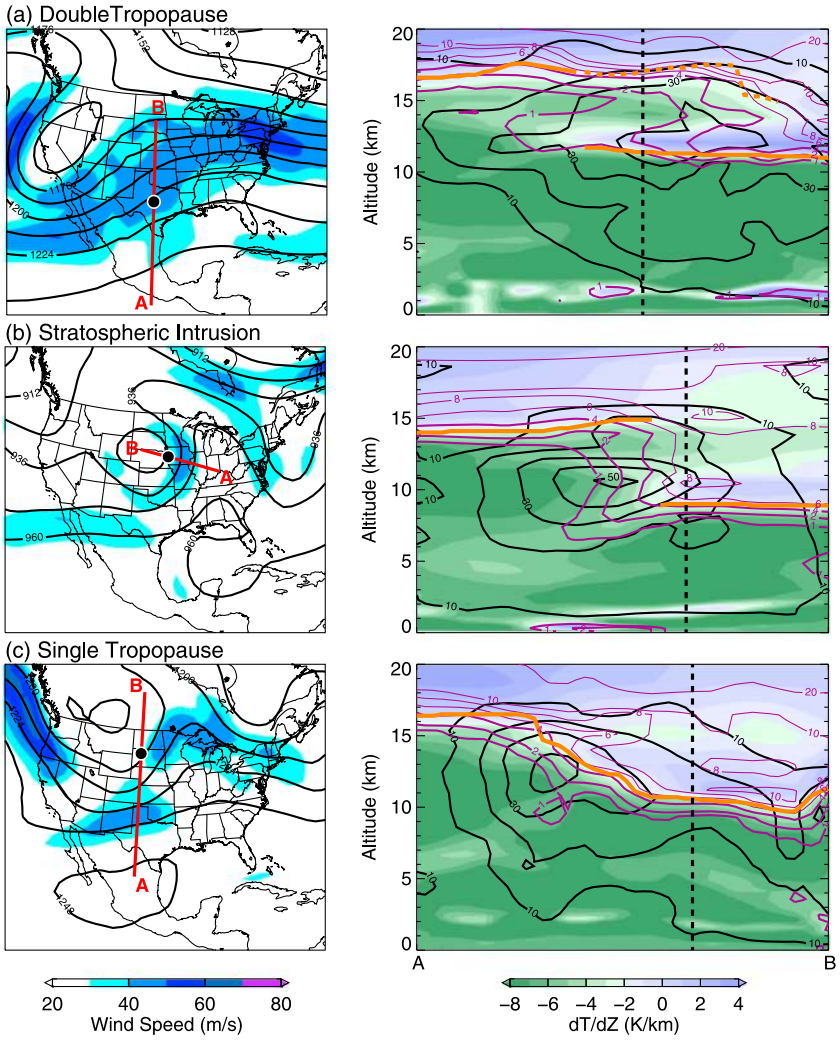

Figure 3. Observed background meteorological states from the ERA-Interim for the (a) double-tropopause case valid at 18 UTC on 8 April 2011, (b) stratospheric intrusion case valid at 18 UTC on 21 May 2011, and (c) single-tropopause case valid at 18 UTC on 18 June 2011. (left) The maps show (in Figures 3a and 3c) 200 hPa wind speed ($m\,s^{-1}$, color fill) and geopotential height (dm, black lines), and (in Figure 3b) 300 hPa wind speed and geopotential height. (right) The vertical sections show the vertical temperature gradient ($K\,km^{-1}$, color fill), wind speed ($m\,s^{-1}$, black lines), potential vorticity (pvu (1 pvu = 10^{-6} $K\,m^2\,kg^{-1}\,s^{-1}$), purple lines), primary tropopause (solid orange lines), secondary tropopause (dashed orange line), and locations of the temperature profiles in Figure 4 (dashed black lines). In each map, the locations of the vertical sections are given by the thick red line labeled "A-B," and the locations of the temperature profiles in Figure 4 are given by the black circle symbols along the red lines.

by the National Weather Service. For deep convection, WSR-88D data are provided by the National Climatic Data Center (NCDC) on native spherical grids every 4–7 min. The methods outlined in *Homeyer* [2014] are used to create three-dimensional composites of the radar data at a horizontal resolution of 0.02° longitude-latitude (~2 km) and 1 km in the vertical. Uncertainty in the altitude of a given convective system from the composite radar data is about 500 m.

For transport analysis, a set of seven passive tropospheric and stratospheric tracers are added to the ARW-WRF model following *Barth et al.* [2012]. In addition to two tracers initialized throughout the depth of the troposphere and the stratosphere, the remaining tracers are initialized in the boundary layer, middle troposphere, upper troposphere, lower stratosphere, and stratospheric overworld. For analysis of convective injection into the lower stratosphere in this study, only one passive tracer is presented: the boundary layer tracer. Little to no transport of middle and upper troposphere tracers above the tropopause was found at any point during simulation for each case. We set the boundary layer tracer to 100% of each grid point

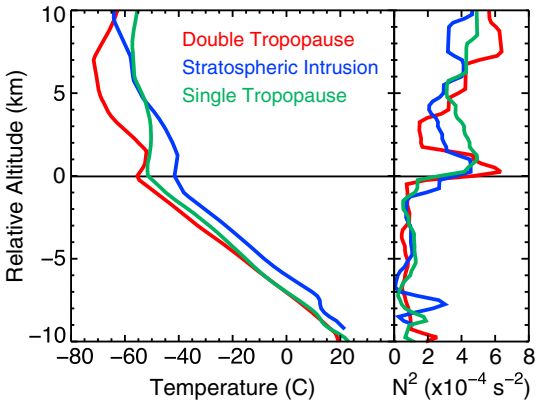

Figure 4. Profiles of (left) temperature and (right) static stability from the ERA-Interim for the double-tropopause case (red), stratospheric intrusion case (blue), and single-tropopause case (green) in relative altitude to the tropopause at the times and locations given in Figure 3.

volume that lies at or below the altitude of the PBL. The tracer is reset at these levels during each model time step (2 s) to provide a continuous source of boundary layer air and to account for diurnal variations in the PBL height. The only pathway for transport of boundary layer air to the stratosphere during each model simulation is through moist convection.

3. Results

3.1. Storm Characteristics

Because the goal of this study is to identify the extent of convective overshooting and transport within various large-scale environments, only model simulations from the nested 3 km domains with explicitly resolved convection are presented below. Although the simulated and observed storms are not expected to be equivalent, several studies have shown that state-of-the-art model simulations with explicitly resolved convection (such as ARW-WRF) on horizontal grid scales less that 4 km are often capable of reproducing the location, horizontal scale, and evolution of observed mesoscale convective systems (MCSs), though additional factors such as the timing and associated precipitation can show significant biases [e.g., *Done et al.*, 2004; *Trier et al.*, 2012] Figure 5 shows observations of column-maximum radar reflectivity from the NEXRAD WSR-88D network and that simulated in the ARW-WRF model using the Morrison and Thompson BMPs during mature stages of the targeted convective systems for each of the three large-scale stability cases. The times of the observed and simulated fields are equivalent, and the targeted convective systems are identified by the black ellipses in each case. Despite some expected differences in the timing and location of the simulated storms, the extent and orientation of each system compare well with observations. For the double-tropopause case (Figure 5a), the simulation with the Morrison BMP correctly predicts the evolution of one MCS that splits into two distinct MCSs: one that continues to travel north and east and another that travels primarily eastward. Although this predicted evolution is correct, the observations illustrate that the timing of the MCS split occurs too early in the simulation. The simulation of the double-tropopause case with the Thompson BMP, however, does not produce the observed split and evolution of two distinct MCSs, with the southern portion of the system collapsing several hours prior to the given analysis time. For the stratospheric intrusion case (Figure 5b), both BMPs predict a system with similar structure: a large leading-line trailing-stratiform MCS to the north and a smaller convective line to the south and east. The observations show that although the targeted convective system had similar structure, the northern and southern components of the convective line have less asymmetry. For the single-tropopause case (Figure 5c), the orientation and structure of the simulated storms from each BMP are nearly identical but differ from observations in the scale and organization of the targeted convective system. The observed system is split into two distinct convective systems with clear separation in latitude, while the simulated systems are more continuous with a smaller latitudinal extent.

An understanding of the vertical extent of the simulated convection is critical for evaluating the ability of the ARW-WRF model to represent potential injection of tropospheric air into the lower stratosphere. For each convective system, the three-dimensional NEXRAD WSR-88D composites provide an observed representation of the vertical extent of each storm that can be compared to simulated reflectivity and cloud fields from ARW-WRF. Because the NEXRAD WSR-88D systems are not capable of sensing the cloud top, they provide underestimations in the altitude of the observed storms which are expected to be small near deep convection (< 500 m) and larger in the trailing-stratiform and anvil regions where detectable hydrometeors gradually settle [e.g., see *Homeyer*, 2014, Figure 6]. Figure 6 shows frequency distributions of the maximum altitude of the 10 dBZ radar reflectivity surface from NEXRAD WSR-88D observations and ARW-WRF simulations, the ARW-WRF simulated cloud top, and the mean altitude of the primary lapse-rate tropopause within 450 km × 450 km boxes centered on the location of the identified convective systems (similar to the ellipses in Figure 5). These altitude distributions are for a single observation during stages of mature

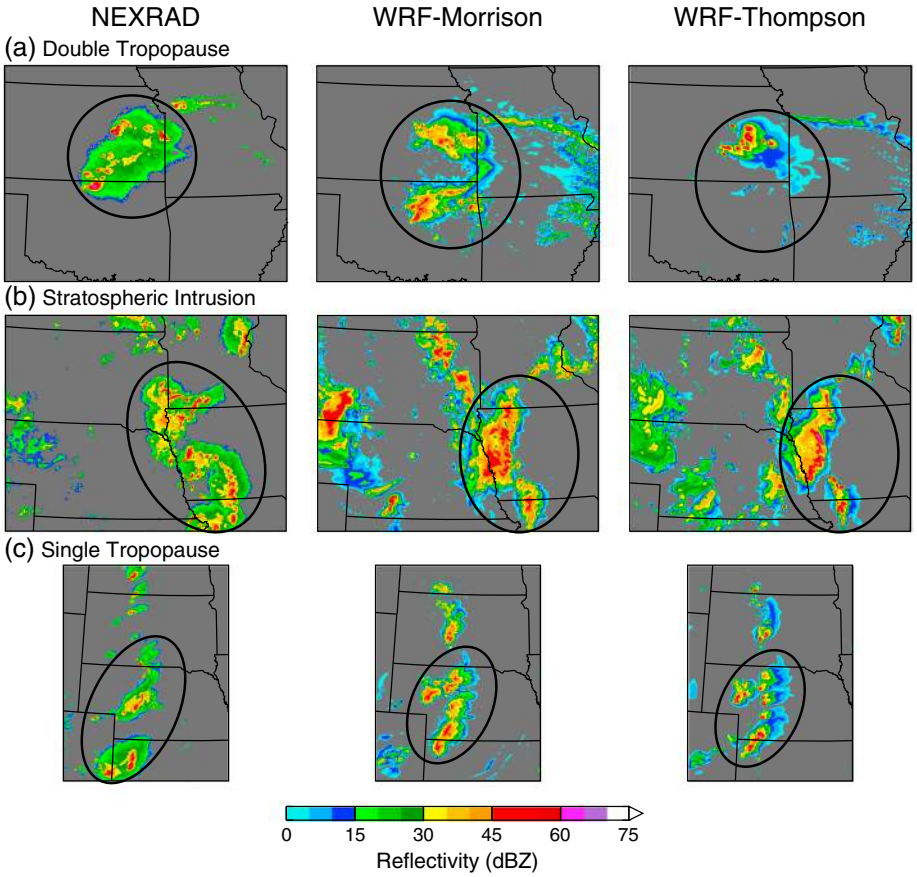

Figure 5. Maps of column-maximum radar reflectivity during select times of mature, tropopause-penetrating convection from (left) composite NEXRAD WSR-88D observations, (middle) ARW-WRF simulations with the Morrison BMP, and (right) ARW-WRF simulations with the Thompson BMP for the (a) double-tropopause case valid at 03 UTC on 9 April 2011, (b) stratospheric intrusion case valid at 02 UTC on 22 May 2011, and (c) single-tropopause case valid at 00 UTC on 19 June 2011. The storm systems analyzed in this study are identified within the black ellipses in each panel.

tropopause-penetrating convection for each case (see figure caption for exact date and time), and distributions of the observed and simulated storm top altitude variables at additional times during the mature stages of each storm are comparable. For all cases, altitude distributions of the simulated radar reflectivity fields largely underpredict the observed distributions. Frequency distributions of the simulated cloud top, however, are centered at altitudes slightly higher than the simulated and observed radar reflectivity fields, in agreement with the limitations of the radar observations outlined above.

The storm top altitude distributions in Figure 6 illustrate that the ARW-WRF model is capable of simulating representative depths of convection in overshooting storms. There are apparent limitations, however, in the representation of the storm top that differ between large-scale environments and BMPs. Frequency distributions of the storm top from ARW-WRF simulations with the Thompson BMP are found at lower altitudes than from simulations with the Morrison BMP for all cases. The largest differences in distributions of the simulated and observed radar reflectivity fields are found for the double-tropopause case (Figure 6a). Underprediction of the vertical extent is larger for the Thompson BMP, which shows a much broader frequency distribution and a peak 4 km below that observed. The Morrison BMP also underpredicts the 10 dBZ reflectivity height but shows two peaks in the frequency distribution, one within 1 km of that observed and the other 5 km below. Frequency distributions of the cloud top height for the double-tropopause case, however, exceed that observed from radar at all altitudes above the tropopause for the simulation with the Morrison BMP, while the highest altitudes are underrepresented in the simulation with the Thompson BMP. For the stratospheric intrusion case (Figure 6b), simulations with the Thompson and Morrison BMPs are comparable, with a slight underprediction of the peak in the observed altitude distribution ranging from 1 to 2 km. Frequency

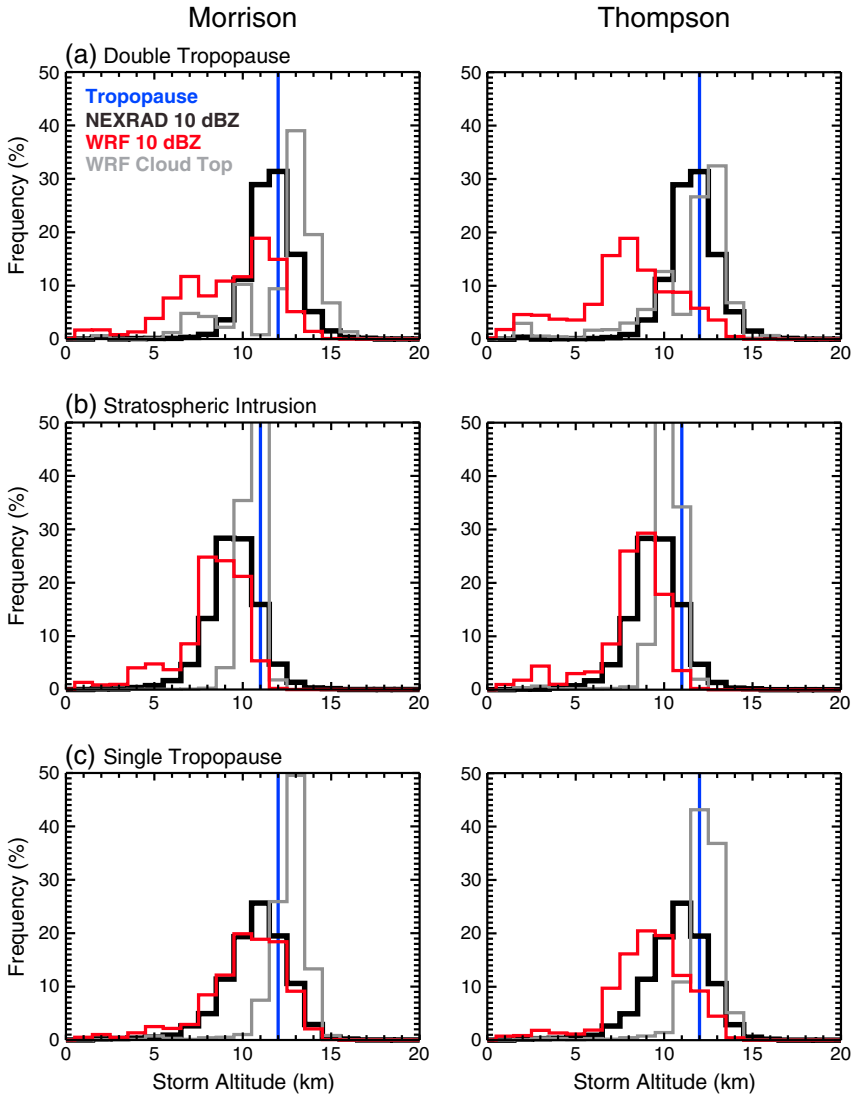

Figure 6. Frequency distributions of the maximum grid point altitude of the 10 dB*Z* reflectivity surface from NEXRAD WSR-88D observations (black lines) and the 10 dB*Z* reflectivity surface and cloud top (particle concentration $\geq$ 0.1 per liter) from ARW-WRF simulations (red and gray lines, respectively) for the (a) double-tropopause case valid at 00 UTC on 9 April 2011, (b) stratospheric intrusion case valid at 01 UTC on 22 May 2011, and (c) single-tropopause case valid at 01 UTC on 19 June 2011. For the ARW-WRF variables, simulated fields with the Morrison (left column) and Thompson BMPs (right column). The blue vertical lines in each panel show the mean lapse-rate tropopause altitude from the ARW-WRF simulations.

distributions of the cloud top for the stratospheric intrusion case also show that the simulated convective systems do not reach the highest altitudes observed by radar which, as outlined above, are likely to be underestimations of the true cloud top. This underrepresentation of the maximum simulated vertical extent of the convective system for the stratospheric intrusion case is at least 2 km. For the single-tropopause case (Figure 6c), the ARW-WRF simulation with the Morrison BMP shows altitude frequency distributions consistent with the observations, while altitude distributions from the simulation with the Thompson BMP underpredict the observed vertical extent, especially for the simulated radar reflectivity field.

Following examination of the fidelity of model simulations for producing representative depths and scales of the observed convective systems above, the remaining analysis of the three case studies is largely restricted to model simulations with the Morrison BMP. Unless otherwise noted, results from ARW-WRF simulations with the Thompson BMP are comparable.

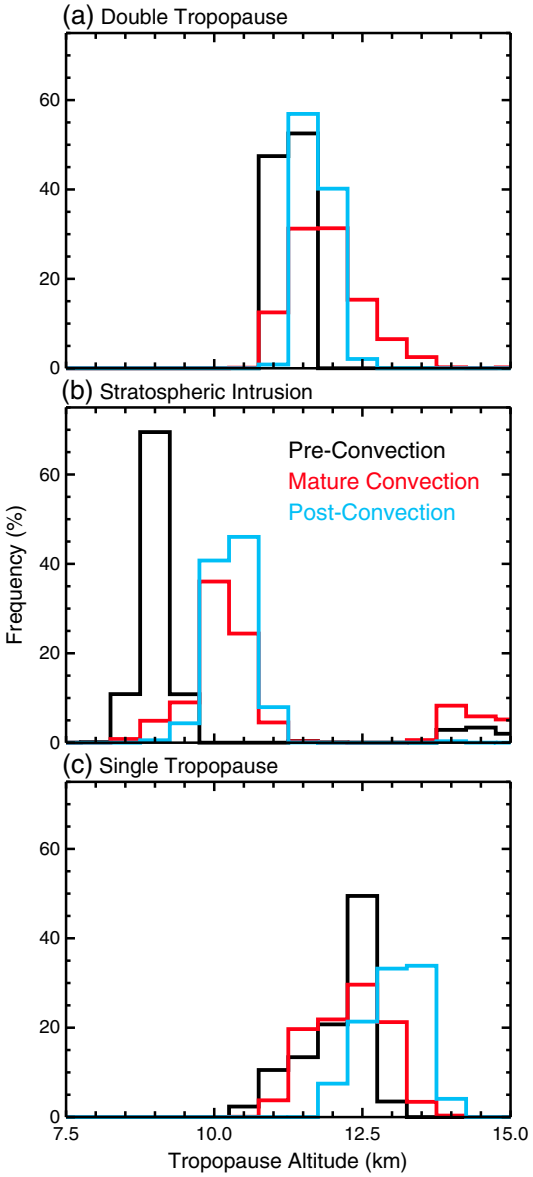

Figure 7. Frequency distributions of the lapse-rate tropopause altitude in ARW-WRF simulations with the Morrison BMP from preconvection (black lines), mature convection (red lines), and postconvection (blues lines) states for the (a) double-tropopause case, (b) stratospheric intrusion case, and (c) single-tropopause case.

3.2. Tropopause Modification

Because the tropopause represents a boundary between tropospheric and stratospheric air and diagnosing transport into the lower stratosphere requires its identification, an understanding of the variability and modification of the altitude of the tropopause within the environment of the convective system in ARW-WRF simulations is needed. Figure 7 shows frequency distributions of the altitude of the tropopause within moving storm-centered 450 km × 450 km boxes (as in Figure 6) during preconvection (2 h before the first tropopause-penetrating convection), mature convection (time of deepest tropopause-penetrating convection), and postconvection states (2 h following tropopause-penetrating convection). In the postconvection state, the vertical extent of any residual convective system is limited to altitudes several kilometers below the tropopause. We choose a time of 2 h following tropopause-penetrating convection in this case to avoid additional dynamical modification of the targeted convective environment from nonconvective processes during the remainder of the simulation.

For all cases, the frequency distributions show clear modification of the altitude of the tropopause between preconvection and postconvection states. In addition, the distributions are broadest during the mature convection states, indicating contributions from rapid modification near active convection and the relatively unperturbed environment outside of the convective systems. Mean increases in the altitude of the tropopause following tropopause-penetrating convection are smallest for the double-tropopause case (~500 m) and largest for the stratospheric intrusion case (~1.5 km), with increases of ~1 km for the single-tropopause case. For the stratospheric intrusion case (Figure 7b), a small peak in the frequency distribution is observed near altitudes of 14 to 15 km. This secondary peak represents a portion of the large-scale environment on the anticyclonic (subtropical) side of the jet and is not representative of processes near the analyzed convective system.

The primary mechanism responsible for modification of the tropopause altitude does differ between large-scale stability cases. Two primary mechanisms are considered here: erosion of the preconvection tropopause layer from convective mixing and diabatic heating of the atmospheric column. Examination of the passive tracers initialized in the stratosphere shows extensive downward transport into the troposphere within the convective system for the stratospheric intrusion case, suggesting that mixing is a primary mechanism (not shown). Alternatively, downward mixing of stratospheric air is not observed in the single- and double-tropopause cases, suggesting that diabatic heating is the primary mechanism for elevating the tropopause in those cases.

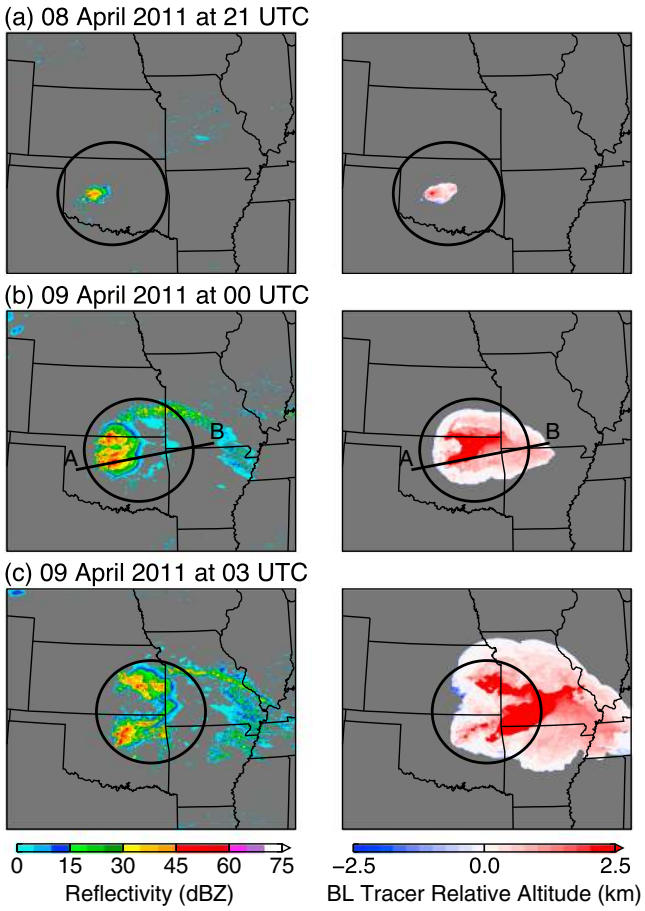

Figure 8. Maps of column-maximum radar reflectivity and the maximum altitude of nonzero boundary layer (BL) tracer fractions (≥1%) relative to the altitude of the lapse-rate tropopause from the ARW-WRF simulation with the Morrison BMP of the double-tropopause case valid at (a) 21 UTC on 8 April 2011, (b) 00 UTC on 9 April 2011, and (c) 03 UTC on 9 April 2011. The storm system analyzed in this study is identified within the black ellipses at each time.

3.3. Transport Characteristics
3.3.1. Evolution

In order to illustrate the evolution of the simulated convective systems and associated transport, snapshots of column-maximum radar reflectivity and the maximum altitude of nonzero boundary layer tracer (≥ 1%) relative to the altitude of the tropopause are shown. Figure 8 shows the evolution of the targeted convective system for the double-tropopause case. The evolution from one MCS that splits into two distinct systems, discussed previously in reference to Figure 5, is clearly observed in Figures 8a–8c. Transport of boundary layer air above the tropopause is evident in the earliest stages of the storm, showing two primary sources of injection exceeding 2.5 km in altitude above the tropopause from the northern and southern elements of the initial convective system. The horizontal scale of these injected plumes increases with increasing distance from the convective source due to both the splitting MCS evolution and the advection and mixing of the injected air into the lower stratosphere.

Figure 9 shows the evolution of the targeted convective system for the stratospheric intrusion case. The convective system of interest in this case is preceded by numerous convective systems within the domain that transport boundary layer air near and slightly above the tropopause. Vertical transport of boundary layer air within the targeted convective system, however, extends to higher altitudes above the tropopause than the adjacent systems during its life cycle. The maximum relative altitudes of injection for the stratospheric intrusion case are lower than the plumes observed in the double-tropopause case but do reach altitudes up to 2 km above the tropopause. Because the stratospheric intrusion and convection in this case are associated with a large upper tropospheric cyclone moving from west to east over South Dakota during the simulation time period, the transported boundary layer air is routinely advected and mixed into the center of the

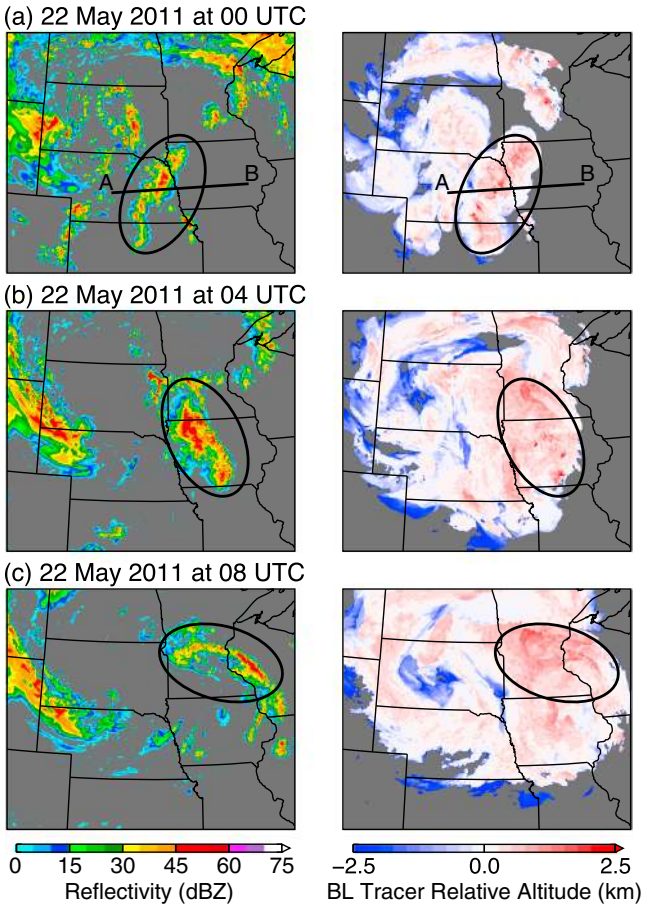

Figure 9. As in Figure 8 but for the stratospheric intrusion case valid at (a) 00 UTC on 22 May 2011, (b) 04 UTC on 22 May 2011, and (c) 08 UTC on 22 May 2011.

cyclonic circulation. Despite the apparent complexity introduced by the upper tropospheric cyclone in this case, the circulation acts to confine the injected boundary layer air into a distinct sector for further analysis.

Figure 10 shows the evolution of the targeted convective system for the single-tropopause case. Similar to the stratospheric intrusion case, the targeted convective system in the single-tropopause case is preceded and followed by additional near-tropopause convective systems within the model domain. In this case, however, transport of injected boundary layer air in the adjacent systems is directed to the east and north and away from the targeted convective system. The maximum above-tropopause altitudes of injected boundary layer air in this case reach similar levels to the double-tropopause case but do not remain at equivalent levels away from their source regions. Such an evolution in tropopause-relative altitude may be related to the modification of the UTLS and tropopause by the convective storm, as discussed previously in section 3.2 and illustrated in Figure 7.

3.3.2. Vertical Structure

Vertical cross sections through some of the deepest convective elements of the simulated systems shed further light on the transport characteristics for each case. Figures 11–13 show vertical cross sections of the potential vorticity (PV), the vertical gradient of potential temperature (a measure of static stability), and the fraction of air originating in the boundary layer, respectively. The locations of vertical sections for each case are shown as the thick black lines labeled "A-B" in Figures 8b, 9a, and 10b. Although these vertical cross sections represent each storm at a single-model time step, there are general characteristics of interest that are present throughout each simulation. In particular, all cases show characteristics suggestive of gravity wave breaking on the downstream edge of the overshooting top, illustrated by moderate (up to 500 m) undulations in the altitude of potential temperature contours and large gradient reversals of PV in altitude. In addition, variations in the static stability from tropospheric ($< 10\,\mathrm{K\,km^{-1}}$) to stratospheric ($> 10\,\mathrm{K\,km^{-1}}$) values above the tropopause further reveal these wave-breaking features. It is important to note here that

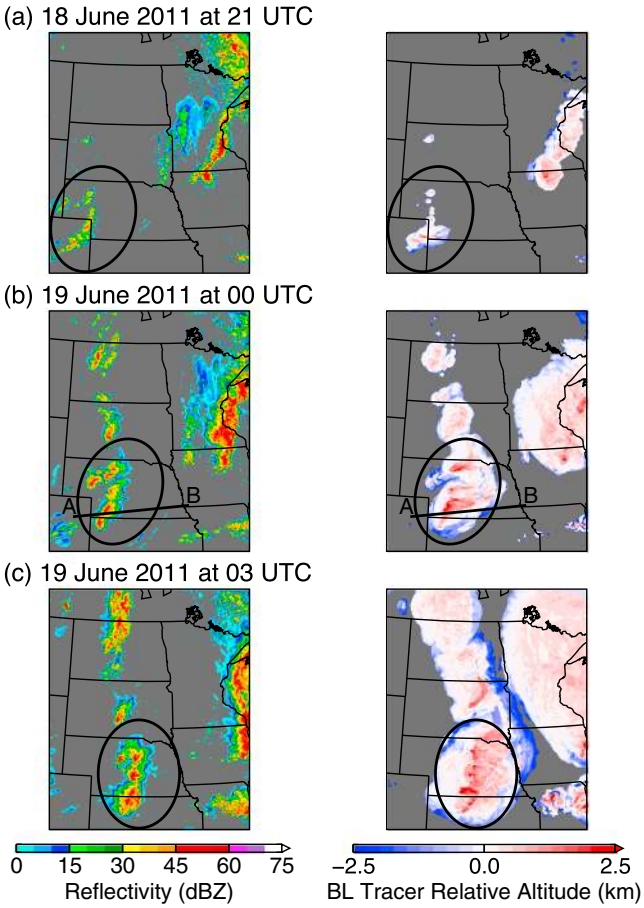

Figure 10. As in Figure 8 but for the single-tropopause case valid at (a) 21 UTC on 18 June 2011, (b) 00 UTC on 19 June 2011, and (c) 03 UTC on 19 June 2011.

because vertical mixing is accomplished in the ARW-WRF simulations by the PBL scheme, unstable layers (vertical overturning of potential temperature contours) are rapidly mixed away, preventing direct diagnosis of gravity wave breaking in the model output fields in some cases.

The vertical cross sections of boundary layer tracer (Figure 13) reveal distinct differences in transport and mixing of boundary layer air into the lower stratosphere between the three large-scale cases. The double-tropopause case (Figure 13a) shows deep injection and direct mixing of the overshooting top into the lower stratosphere near 15 km in altitude and 390 K in potential temperature, evident in the cloud and tracer fields. This direct mixing corresponds to the distinct tracer plumes observed above the tropopause throughout the evolution of the convective system in Figure 8. Such direct mixing is not observed in the stratospheric intrusion and single-tropopause cases, where the cloud top is largely restricted to the altitude of the lapse-rate tropopause and boundary layer air above the tropopause is limited to potential temperatures below 370 K.

Variability in the altitude of the tropopause as diagnosed from the changing width of the altitude distribution in Figure 7 and discussion in section 3.2 is shown in the vertical cross sections to be contained within the cloud field of the convective systems. In particular, the altitude of the tropopause (black dots in Figures 12 and 13) is severely disrupted within the region of the overshooting top in each case, with distinct breaks (or jumps) of up to 3 km in altitude. Additional variability in the altitude of the tropopause away from the overshooting top is primarily associated with shallow layered stability features in the upper anvil of each storm, likely from prior wave breaking near the cloud top. One additional unique feature near the tropopause is observed in the double-tropopause case, where the downstream anvil shows a large dipole PV structure near 12 km in altitude. This PV structure is suggestive of diabatic cooling and is present in the downstream anvil of both splitting MCSs at initiation and throughout the period of convective overshooting

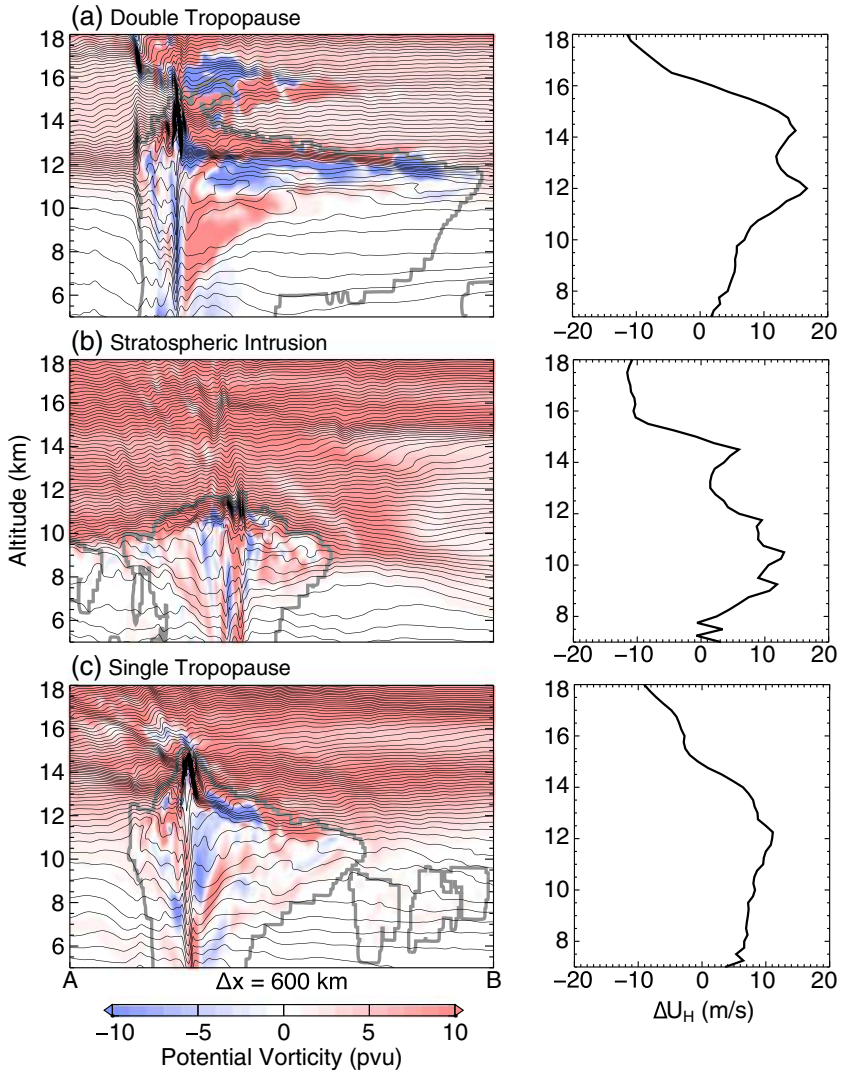

Figure 11. (left) Vertical cross sections of potential vorticity (pvu, color fill), contours of potential temperature θ at 2 K intervals (black lines), and cloud boundaries (gray lines, particle concentration equal to 0.1 per liter) from ARW-WRF simulations with the Morrison BMP along the path "A-B" shown in (a) Figure 8b for the double-tropopause case, (b) Figure 9a for the stratospheric intrusion case, and (c) Figure 10b for the single-tropopause case. (right) Vertical profiles of the horizontal wind for the domain of each vertical section, given as the anomaly relative to the vertical profile mean.

(not shown). Such continued widespread diabatic cooling could explain why modification of the tropopause altitude in the double-tropopause case is small.

Despite the outlined evidence of gravity wave breaking for each case, the time resolution of the output fields (1 h) does not enable further evaluation of the detailed wave activity and potential wave-driven mixing, which typically requires output at time intervals less than about 5 min. The PV and stability fields in the cross sections, however, do show significant differences between the three large-scale stability environments that may imply differences in wave activity. For the stratospheric intrusion and single-tropopause cases, there is little modification of PV and lower stratosphere stability downstream of the overshooting top. However, for the double-tropopause case, there is a layer of deep vertical gradient reversal in PV that corresponds with complex laminar stability structure bounding the portion of the overshooting top being actively mixed near 15 km and extending several hundred kilometers horizontally above the downstream anvil. This unique PV and stability structure suggests that the layer of near tropospheric levels of stability in the lower stratosphere may have facilitated wave breaking that penetrates deeper into the stratosphere, though the potential temperature contours do not suggest active wave breaking at the analyzed

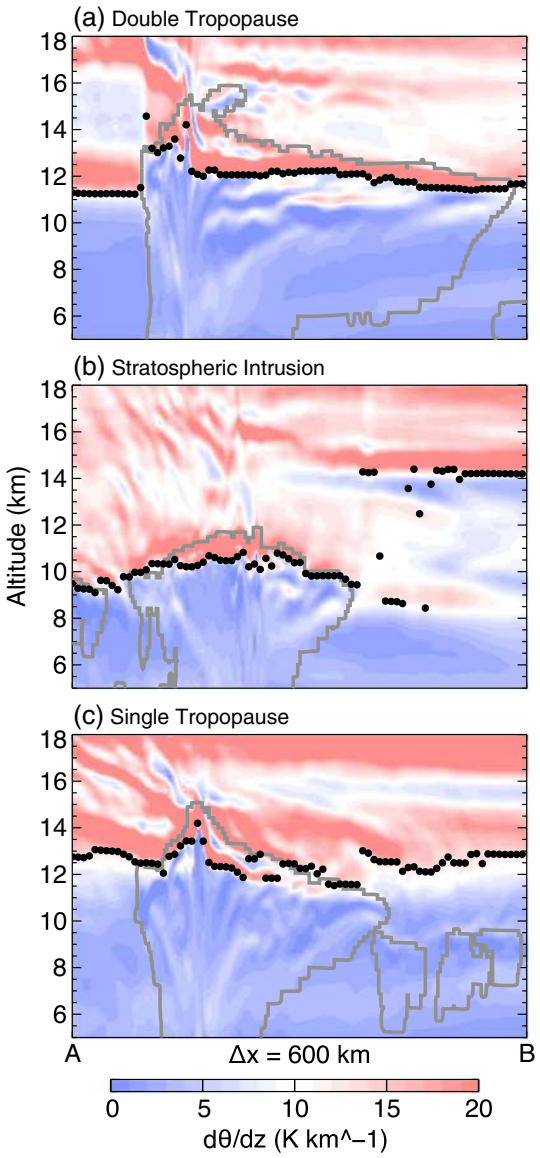

Figure 12. As in Figure 11 but vertical cross sections of the static stability as the vertical gradient of potential temperature θ (K km^{-1}, color fill) and the lapse-rate tropopause altitude (black dots).

model time step. This vertical mixing in the double-tropopause case is characteristically different than that observed in lower stratosphere environments with higher stability.

Following that outlined in *Lane et al.* [2003], gravity waves will break where the wind speed increases or decreases by an amount equivalent to the phase speed of the wave (typically ±15–20 m s^{-1} for the smallest scale waves possible at the model resolution used in this study) relative to the wind speed at the source of the wave, often referred to as a "critical level." Because wavelength is directly related to phase speed, unique critical levels exist for the entire spectrum of waves generated in convection. In order to examine whether the direct mixing observed at 15 km in the double-tropopause case is associated with a critical level, profiles of the horizontal wind speed for the domain of the vertical sections are given in Figure 11 as the anomaly relative to the vertical profile mean. If the source of a gravity wave is near the level of the tropopause and overshooting top in the double-tropopause case (~12 km), the wind profile suggests that a critical level (i.e., ±15 m s^{-1} relative to the wind anomaly at 12 km) may exist above 16 km, which is higher than the level of direct mixing in that case. There is, however, evidence of gravity wave breaking upstream of the overshooting top near 16 km. In addition, similar inspection of wind profiles for the single-tropopause and stratospheric intrusion cases does not reveal critical levels near the altitudes of the overshooting top and regions of mixing.

Although diabatic influences from the convective systems and gravity wave activity in the lower stratosphere provide significant modifications to stability, the stability cross sections (Figure 12) show that the initial large-scale differences in stability between the three cases are largely retained in each model simulation. Sustainment of these large-scale lower stratosphere environments in the ARW-WRF simulations enables characterization of their potential influence on the transport properties of the convective systems throughout their life cycle. There is one exception to this sustainment that can be found to the right of the overshooting top in the single-tropopause case. In the stability cross section, there is a low (tropospheric) stability layer near 16 km. This low-stability layer is not present at the model initialization time step and is sourced by wave activity near the subtropical jet in the southeastern portion of the 3 km ARW-WRF nested domain several hours into the simulation (not shown). Following its source, the low-stability layer expands slightly and rapidly decays after the time of the vertical cross section but never extends fully over the analyzed convective system. Furthermore, although it is possible that the convective line interacted with this low-stability layer during the model simulation, inspection of the hourly output files suggests that convection was never deep enough to penetrate the layer.

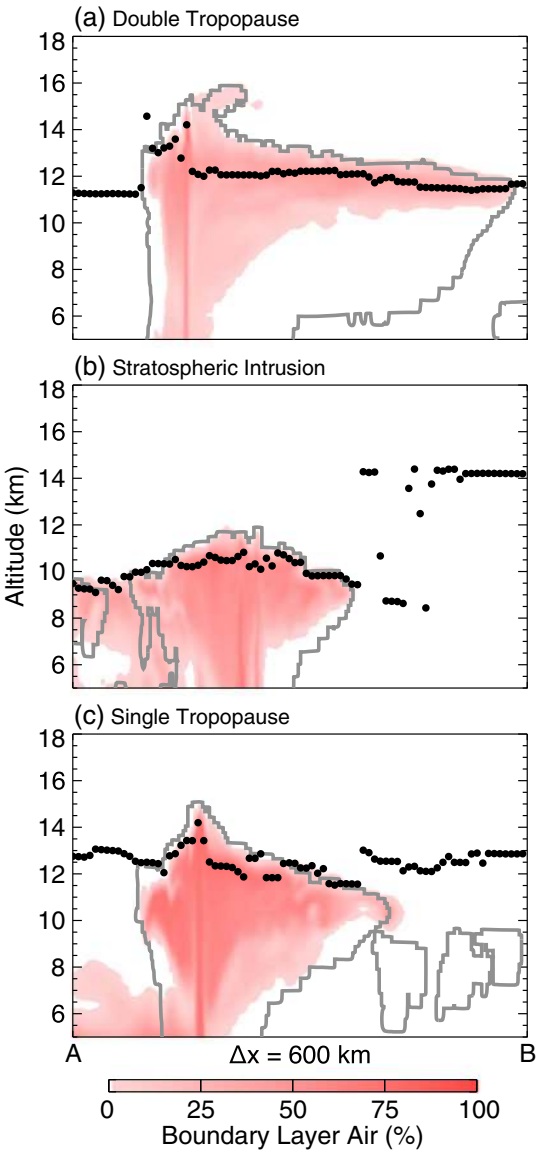

Figure 13. As in Figure 11 but vertical cross sections of the boundary layer tracer (%, color fill) and the lapse-rate tropopause altitude (black dots).

3.3.3. Irreversibility

Analyses of the evolution and mature stages of transport in the simulated convective systems shed light on the characteristics and mechanisms responsible for injection of tropospheric air into the lower stratosphere, but its irreversibility requires analysis of the tracer fields following the decay of responsible convective systems and associated thermodynamical modification of the UTLS. In order to develop an understanding of the qualitative characteristics of irreversible transport for each case (i.e., the vertical extent), the area fraction of the 450 km × 450 km storm environment in the postconvection state (2 h following tropopause-penetrating convection) that contains nonzero boundary layer tracer at altitudes relative to the tropopause is shown in Figure 14 for ARW-WRF simulations with each BMP. At the initial model state, the fraction of boundary layer air at the relative altitudes presented in each profile is 0%. In other words, all boundary layer air observed at these altitudes during the simulation is sourced by convection.

In general, ARW-WRF simulations with either BMP produce qualitatively similar transport profiles for each large-scale stability case. The greatest differences between BMPs are observed near the tropopause for the double-tropopause case, where the Thompson BMP shows much less transport. This is largely a result of only half of the observed convective system predicted in the ARW-WRF simulation with the Thompson BMP, as this simulation did not predict splitting storms (see section 3.1). Apart from underestimation near the tropopause, simulations with each BMP for the double-tropopause case do show qualitatively similar transport into the lower stratosphere. There are also distinct differences in the vertical extent of transport between the three cases. Convective injection is deepest for the double-tropopause case, with boundary layer air at altitudes up to 4 km above the primary lapse-rate tropopause. The vertical extent of transport for the stratospheric intrusion and single-tropopause cases, however, is limited to altitudes below ~2 km above the lapse-rate tropopause. The fraction of the convective environment influenced by boundary layer air is slightly higher near 2 km above the tropopause for the single-tropopause case. In addition to transport above the tropopause, the level of maximum detrainment (largest boundary layer influence) for the double-tropopause case coincides with the altitude of the lapse-rate tropopause, while that for the stratospheric intrusion and single-tropopause cases lies from 1 to 3 km below the tropopause.

It is worth noting here that we expect contributions to cross-tropopause transport from numerical diffusion to be negligible. Because transport of boundary layer air into the upper troposphere and lower stratosphere is achieved through convection, diffusion of boundary layer air between the tropopause level and those above in the lower stratosphere is only possible following prior convective transport. In the ARW-WRF simulations, vertical diffusion is computed at all altitudes by the PBL parameterization. For altitudes near

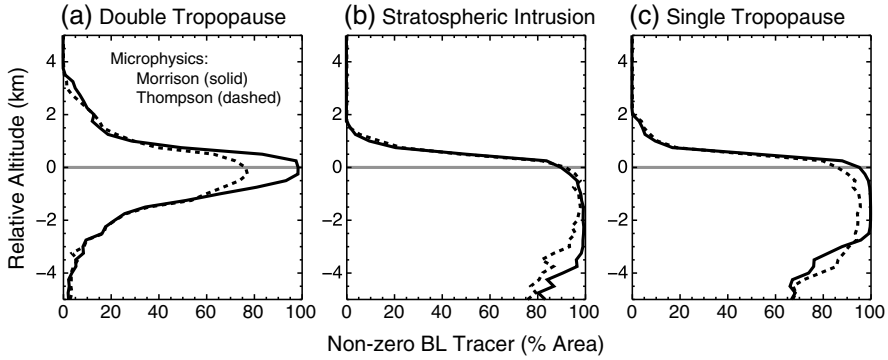

Figure 14. Profiles in relative altitude to the lapse-rate tropopause of the fraction of air with nonzero (≥1%) contributions from the planetary boundary layer in the ARW-WRF simulations within 450 km × 450 km boxes centered on the tracer plume in the postconvection state for the (a) double-tropopause case, (b) stratospheric intrusion case, and (c) single-tropopause case. Dashed lines show results from simulations with the Thompson BMP and solid lines the Morrison BMP.

the tropopause, vertical diffusion is only a function of the Richardson number and the horizontal wind shear. Following examination of the boundary layer tracer and meteorological fields near the tropopause in each case, we estimate the minimum time scale for cross-tropopause transport of nonzero boundary layer tracer (1%) from numerical diffusion to be 1–2 h. These long time scales for vertical diffusion limit transport to altitudes within one model grid point (200 m) of the convectively lofted tracer during the simulation time period.

4. Summary and Discussion

Simulations of explicitly resolved convection from the ARW-WRF numerical model were used to examine the influence of the large-scale environment on the injection of tropospheric air into the extratropical lower stratosphere by moist convection. Observed cases of tropopause-penetrating convection with comparable magnitudes of CAPE were identified for three distinct large-scale lower stratosphere stability environments: double tropopause, stratospheric intrusion, and single tropopause. The model simulations were shown to largely reproduce the characteristic vertical extent of each convective system. In addition, the simulations show that the influence of the large-scale environment on convective injection into the UTLS is significant and largely independent of the microphysics parameterization used. Convective injection of tropospheric air into the lower stratosphere was found to be deepest in simulations of the double-tropopause case, at altitudes up to 4 km above the lapse-rate tropopause (390 K potential temperature). Transport in the remaining cases, for which the lower stratosphere stability is larger, is limited to altitudes less than 2 km above the tropopause (370 K potential temperature).

One goal of this study was to test the dependence of the vertical extent and evolution of simulated convection on the parameterization of cloud microphysics. Two BMPs that predict equivalent hydrometeor classifications were used: a single-moment BMP (Thompson) and a double-moment BMP (Morrison). Comparisons of the simulated horizontal radar reflectivity and cloud top altitudes with high-resolution ground-based radar observations reveal important limitations of the model simulations that require further attention in future studies. In particular, simulated radar reflectivity fields largely underrepresent the observed vertical extent, with the largest differences observed for the double-tropopause case. The simulated cloud top, however, is generally found at or slightly above radar observations of the vertical extent of each convective system, consistent with expected differences between the radar reflectivity fields and the true cloud top. These comparisons suggest that the apportionment of water into the various hydrometeor classifications in the BMP used may not be representative of the observed hydrometeor distributions in the upper levels of deep convective storms. Since the radar reflectivity fields are most sensitive to large hydrometeor classifications (rain, graupel, and snow), the differences observed in this study suggest that the microphysical parameterizations predict excessive cloud ice at these levels. These characteristics are not only important for understanding convective transport and mixing of water vapor into the UTLS, but they also impact the radiative properties of convective clouds. Improving the vertical extent and

distribution of these hydrometeors may also lead to significant improvements in simulating the evolution of deep convection and precipitation.

Thermodynamical modification of the local environment by each convective system and its effect on the level of the tropopause, which is an important consideration for evaluating STE, showed significant differences between the three large-scale cases. In particular, the altitude of the tropopause increased significantly for the stratospheric intrusion case from 9 to ~10.5 km, where the stability transition at the tropopause in the absence of deep convection is broadest. In comparison, increases in the altitude of the tropopause were smallest for the double-tropopause case, which may in part explain the deeper levels of convective injection reached compared to the remaining cases. For example, if the initial level of the tropopause and maximum altitude of convection was equivalent in each case, differences in the elevation of the convectively modified tropopause would correspond directly to differences in the depth of transport above the tropopause.

Apart from the vertical extent of convective injection into the lower stratosphere, the double-tropopause case involved distinct transport characteristics not found in the remaining cases. In particular, Figures 8 and 13 show that the transport to higher above-tropopause altitudes in the double-tropopause case is related to direct mixing of the overshooting convective top into the lower stratosphere at those levels. One factor that could contribute to deeper levels of injection is differences in the intensity of convective updrafts between the three cases. We examined profiles of vertical velocity and vertical kinetic energy within convective updrafts for each case, which did reveal small differences in updraft strength (not shown). In particular, the double-tropopause case contained the strongest updrafts at altitudes within 1 km of the tropopause, with relative differences of up to 30% compared to the remaining cases. These differences in updraft intensity alone, however, can not fully explain such large differences in the depth of injection and the characteristics of mixing. Because the decrease in stability and temperature above the primary tropopause in the double-tropopause case is large, the direct mixing at higher altitudes could be a result of the overshooting convective top reaching a secondary level of neutral buoyancy, encouraging detrainment and mixing of the convectively lofted air mass at these levels. Such a level is supported from inspection of the vertical structure of the cloud field, which shows horizontal downstream-oriented structure near the maximum altitude of the overshooting top (see Figure 13a). Additional simulations of overshooting convection within each large-scale environment are required to identify the relative roles of updraft strength near the tropopause and the vertical structure of lower stratosphere stability for achieving deeper transport in the double-tropopause case.

One additional possibility for the occurrence of deeper injection in the double-tropopause case is that wave activity within the lower environmental stability is characteristically different than that in the cases with higher lower stratosphere stability, which is supported by the vertical cross sections of PV and static stability in Figures 11a and 12a. Due to limited temporal resolution of the simulated fields, it is not known whether the dynamics of the direct mixing in the double-tropopause case differ compared to mixing at lower altitudes near the tropopause and that in the remaining cases. However, there is evidence of gravity wave breaking near the overshooting convective top for all cases, supporting the key role of this process for troposphere-to-stratosphere transport in overshooting convection. Despite evidence of wave breaking within the overshooting top, inspection of the horizontal wind profile above the storm did not suggest that the layer of direct mixing near 15 km in the double-tropopause case was coincident with a critical level where gravity wave breaking is expected to be prevalent. Contours of potential temperature in the mixed layer also did not suggest active wave breaking. Retention of model simulations, and in particular the model mixing parameters, at higher spatial and temporal resolution in future studies may help to shed further light on the responsible transport mechanisms and dynamical characteristics in each case.

Two unknown factors in the simulations completed in this study are the importance of the model resolution and the input data set used. The ERA-Interim reanalysis was chosen for model initialization because of the higher vertical resolution available compared to alternative reanalyses and operational forecast model analyses. Although not shown, limited examination of simulations that were initialized with fields from an analysis with lower vertical resolution and higher horizontal resolution than the ERA-Interim revealed that the vertical extent and associated transport of the targeted convective systems extended to lower altitudes above the tropopause in each of the three cases presented in this study. These limited analyses suggest that the vertical resolution of the initial state, especially in the UTLS region, may be an essential component

that determines the ability of the model to predict representative convective structure and transport across the tropopause. Independent data assimilation of operational radiosondes and other meteorological data to a higher-resolution vertical grid may be necessary for further improvement of the model simulations. In addition, several recent studies have illustrated that small horizontal grid spacing (O(100 m)) is required for accurate representation of gravity wave spectra and the physical process of cloud turbulence [e.g., *Bryan et al.*, 2003; *Lane and Knievel*, 2005; *Bryan and Morrison*, 2012]. Although model resolution is an important consideration, the sensitivity of the qualitative aspects of transport identified in this study to horizontal resolution, as outlined in section 2, is not known. If gravity wave spectra were to change significantly for smaller grid spacing in the cases presented, preferred altitudes of wave breaking (critical levels) and associated transport may also change. Further studies are needed to fully examine the dependence of qualitative and quantitative aspects of transport on model resolution for overshooting convection.

It is worth noting that the simulations in this study do not suggest that transport to levels greater than 2 km above the tropopause is only possible for cases with a double tropopause. As outlined in section 2, the selected large-scale cases were chosen in part because their environments are characterized by similar magnitudes of CAPE, which is a common metric used for predicting and classifying convective intensity [e.g., *Rasmussen and Blanchard*, 1998]. For example, if the CAPE was significantly larger in the single-tropopause or stratospheric intrusion case, convective updrafts would likely be stronger and capable of lofting air to higher altitudes before becoming neutrally buoyant. The sensitivity of convective overshooting to the stability of the lower stratosphere for comparable levels of CAPE identified in this study, however, suggests that the lower stratosphere stability may be an important factor controlling the depth and occurrence of tropopause-penetrating convection. Further examination of the role these lower stratosphere features play for the injection of tropospheric air into the lower stratosphere in environments with varying levels of CAPE is needed to test the ubiquity of the transport characteristics identified in this study. In particular, the role of double-tropopause events in facilitating deep convective injection and their association with direct mixing of convective overshoots into the lower stratosphere deserves further attention. In addition, all simulations of the stratospheric intrusion case underrepresented the maximum observed vertical extent of the convective system, while those for the double-tropopause and single-tropopause cases were largely in agreement with observations. The vertical depth of injected boundary layer air into the lower stratosphere may therefore be underrepresented in the stratospheric intrusion case. Additional case studies may shed further light on the ability of the model to simulate representative convective systems in large-scale environments with a stratospheric intrusion.

Acknowledgments

We thank the European Centre for Medium-Range Weather Forecasting for providing the ERA-Interim data, which were obtained from the Research Data Archive (RDA) maintained by the Computational and Information Systems Laboratory (CISL) at the National Center for Atmospheric Research (NCAR). The original data are available from the RDA (http://rda.ucar.edu) in data set ds627.0. We also thank Eric Jensen at NCAR, Claudia Stephan at NWRA/CU-Boulder, and Joan Alexander at NWRA for helpful discussions and two anonymous reviewers for their comments and suggestions. The first author also thanks the Advanced Study Program (ASP) at NCAR for postdoctoral support. The National Center for Atmospheric Research is sponsored by the National Science Foundation.

References

Anderson, J. G., D. M. Wilmouth, J. B. Smith, and D. S. Sayres (2012), UV dosage levels in summer: Increased risk of ozone loss from convectively injected water vapor, *Science*, *337*(6096), 835–839.

Barth, M. C., J. Lee, A. Hodzic, G. Pfister, W. C. Skamarock, J. Worden, J. Wong, and D. Noone (2012), Thunderstorms and upper troposphere chemistry during the early stages of the 2006 North American Monsoon, *Atmos. Chem. Phys.*, *12*, 11,003–11,026, doi:10.5194/acp-12-11003-2012.

Birner, T. (2006), Fine-scale structure of the extratropical tropopause, *J. Geophys. Res.*, *111*, D04104, doi:10.1029/2005JD006301.

Birner, T., A. Dörnbrack, and U. Schumann (2002), How sharp is the tropopause at midlatitudes?, *Geophys. Res. Lett.*, *29*(14), 1700, doi:10.1029/2002GL015142.

Bryan, G. H., and H. Morrison (2012), Sensitivity of a simulated squall line to horizontal resolution and parameterization of microphysics, *Mon. Weather Rev.*, *140*, 202–225, doi:10.1175/MWR-D-11-00046.1.

Bryan, G. H., J. C. Wyngaard, and J. M. Fritsch (2003), Resolution requirements for the simulation of deep moist convection, *Mon. Weather Rev.*, *131*, 2394–2416.

Chagnon, J. M., and S. L. Gray (2007), Stratosphere-troposphere transport in a numerical simulation of midlatitude convection, *J. Geophys. Res.*, *112*, D06314, doi:10.1029/2006JD007265.

Chagnon, J. M., and S. L. Gray (2010), A comparison of stratosphere-troposphere transport in convection-permitting and convection-parameterizing simulations of three mesoscale convective systems, *J. Geophys. Res.*, *115*, D24318, doi:10.1029/2010JD014421.

Corti, T., et al. (2008), Unprecedented evidence for deep convection hydrating the tropical stratosphere, *Geophys. Res. Lett.*, *35*, L10810, doi:10.1029/2008GL033641.

Cotton, W. R., G. H. Bryan, and S. C. van den Heever (2011), *Storm and Cloud Dynamics*, 2nd ed., 809 pp., Academic Press, Waltham, Massachusetts.

Crum, T. D., and R. L. Alberty (1993), The WSR-88D and the WSR-88D operational support facility, *Bull. Am. Meteorol. Soc.*, *74*(9), 1669–1687.

Dee, D. P., et al. (2011), The ERA-Interim reanalysis: Configuration and performance of the data assimilation system, *Q. J. R. Meteorolog. Soc.*, *137*, 553–597, doi:10.1002/qj.828.

Dessler, A. E., and S. C. Sherwood (2004), Effect of convection on the summertime extratropical lower stratosphere, *J. Geophys. Res.*, *109*, D23301, doi:10.1029/2004JD005209.

Done, J., C. A. Davis, and M. Weisman (2004), The next generation of NWP: Explicit forecasts of convection using the weather research and forecasting (WRF) model, *Atmos. Sci. Lett.*, *5*, 110–117.

Fischer, H., et al. (2003), Deep convective injection of boundary layer air into the lowermost stratosphere at midlatitudes, *Atmos. Chem. Phys.*, *3*(3), 739–745.

Fromm, M. D., and R. Servranckx (2003), Transport of forest fire smoke above the tropopause by supercell convection, *Geophys. Res. Lett.*, *30*(10), 1542, doi:10.1029/2002GL016820.

Gray, S. L. (2003), A case study of stratosphere to troposphere transport: The role of convective transport and the sensitivity to model resolution, *J. Geophys. Res.*, *108*(D18), 4590, doi:10.1029/2002JD003317.

Hanisco, T. F., et al. (2007), Observations of deep convective influence on stratospheric water vapor and its isotopic composition, *Geophys. Res. Lett.*, *34*, L04814, doi:10.1029/2006GL027899.

Hassim, M. E. E., and T. P. Lane (2010), A model study on the influence of overshooting convection on TTL water vapour, *Atmos. Chem. Phys.*, *10*, 9833–9849, doi:10.5194/acp-10-9833-2010.

Hegglin, M. I., et al. (2004), Tracing troposphere-to-stratosphere transport above a mid-latitude deep convective system, *Atmos. Chem. Phys.*, *4*(3), 741–756, doi:10.5194/acp-4-741-2004.

Holton, J. R., P. H. Haynes, M. E. McIntyre, A. R. Douglass, and L. Pfister (1995), Stratosphere-troposphere exchange, *Rev. Geophys.*, *33*(4), 403–439.

Homeyer, C. R. (2014), Formation of the enhanced-V infrared cloud top feature from high-resolution three-dimensional radar observations, *J. Atmos. Sci.*, *71*, 332–348, doi:10.1175/JAS-D-13-079.1.

Homeyer, C. R., K. P. Bowman, L. L. Pan, E. L. Atlas, R.-S. Gao, and T. L. Campos (2011), Dynamical and chemical characteristics of tropospheric intrusions observed during START08, *J. Geophys. Res.*, *116*, D06111, doi:10.1029/2010JD015098.

Hong, S.-Y., Y. Noh, and J. Dudhia (2006), A new vertical diffusion package with an explicit treatment of entrainment processes, *Mon. Weather Rev.*, *134*, 2318–2341.

Jensen, E. J., A. S. Ackerman, and J. A. Smith (2007), Can overshooting convection dehydrate the tropical tropopause layer?, *J. Geophys. Res.*, *112*, D11209, doi:10.1029/2006JD007943.

Keyser, D., and M. A. Shapiro (1986), A review of the structure and dynamics of upper-level frontal zones, *Mon. Weather Rev.*, *114*, 452–499.

Lane, T. P., and J. C. Knievel (2005), Some effects of model resolution on simulated gravity waves generated by deep, mesoscale convection, *J. Atmos. Sci.*, *62*, 3408–3419.

Lane, T. P., and R. D. Sharman (2006), Gravity wave breaking, secondary wave generation, and mixing above deep convection in a three-dimensional cloud model, *Geophys. Res. Lett.*, *33*, L23813, doi:10.1029/2006GL027988.

Lane, T. P., and R. D. Sharman (2008), Some influences of background flow conditions on the generation of turbulence due to gravity wave breaking above deep convection, *J. Appl. Met. Clim.*, *47*, 2777–2796, doi:10.1175/2008JAMC1787.1.

Lane, T. P., R. D. Sharman, T. L. Clark, and H.-M. Hsu (2003), An investigation of turbulence generation mechanisms above deep convection, *J. Atmos. Sci.*, *60*, 1297–1321.

Le, T. V., and W. A. Gallus (2012), Effect of an extratropical mesoscale convective system on water vapor transport in the upper troposphere/lower stratosphere: A modeling study, *J. Geophys. Res.*, *117*, D03111, doi:10.1029/2011JD016685.

Luderer, G., J. Trentmann, K. Hungershöfer, M. Herzog, M. Fromm, and M. O. Andreae (2007), Small-scale mixing processes enhancing troposphere-to-stratosphere transport by pyro-cumulonimbus storms, *Atmos. Chem. Phys.*, *7*, 5945–5957.

Morrison, H., and J. Milbrandt (2011), Comparison of two-moment bulk microphysics schemes in idealized supercell thunderstorm simulations, *Mon. Weather Rev.*, *139*, 1103–1130, doi:10.1175/2012MWR3433.1.

Morrison, H., G. Thompson, and V. Tatarskii (2009), Impact of cloud microphysics on the development of trailing stratiform precipitation in a simulated squall line: Comparison of one- and two-moment schemes, *Mon. Weather Rev.*, *137*, 991–1007, doi:10.1175/2008MWR2556.1.

Mullendore, G. L., D. R. Durran, and J. R. Holton (2005), Cross-tropopause tracer transport in midlatitude convection, *J. Geophys. Res.*, *110*, D06113, doi:10.1029/2004JD005059.

Pan, L. L., W. J. Randel, J. C. Gille, W. D. Hall, B. Nardi, S. Massie, V. Yudin, R. Khosravi, P. Konopka, and D. Tarasick (2009), Tropospheric intrusions associated with the secondary tropopause, *J. Geophys. Res.*, *114*, D10302, doi:10.1029/2008JD011374.

Poulida, O., R. R. Dickerson, and A. Heymsfield (1996), Stratosphere-troposphere exchange in a midlatitude mesoscale convective complex 1. Observations, *J. Geophys. Res.*, *101*(D3), 6823–6836.

Rasmussen, E. N., and D. O. Blanchard (1998), A baseline climatology of sounding-derived supercell and tornado forecast parameters, *Weather Forecast.*, *13*, 1148–1164.

Ray, E. A., et al. (2004), Evidence of the effect of summertime midlatitude convection on the subtropical lower stratosphere from CRYSTAL-FACE tracer measurements, *J. Geophys. Res.*, *109*, D18304, doi:10.1029/2004JD004655.

Reed, R. J. (1955), A study of a characteristic type of upper-level frontogenesis, *J. Meteorolog.*, *12*, 226–237.

Sherwood, S. C., and A. E. Dessler (2000), On the control of stratospheric humidity, *Geophys. Res. Lett.*, *27*(16), 2513–2516.

Skamarock, W. C., J. B. Klemp, J. Dudhia, D. O. Gill, D. M. Barker, M. G. Duda, X.-Y. Huang, W. Wang, and J. G. Powers (2008), A description of the Advanced Research WRF version 3, *NCAR Tech. Note 475+STR*.

Solomon, S., K. H. Rosenlof, R. W. Portmann, J. S. Daniel, S. M. Davis, T. J. Sanford, and G.-K. Plattner (2010), Contributions of stratospheric water vapor to decadal changes in the rate of global warming, *Science*, *327*, 1219–1223, doi:10.1126/science.1182488.

Stohl, A., H. Wernli, P. James, M. Bourqui, C. Forster, M. A. Liniger, P. Seibert, and M. Sprenger (2003), A new perspective of stratosphere-troposphere exchange, *Bull. Am. Meteorol. Soc.*, *84*(11), 1565–1573.

Tang, Q., M. J. Prather, and J. Hsu (2011), Stratosphere-troposphere exchange ozone flux related to deep convection, *Geophys. Res. Lett.*, *38*, L03806, doi:10.1029/2010GL046039.

Thompson, G., P. R. Field, R. M. Rasmussen, and W. D. Hall (2008), Explicit forecasts of winter precipitation using an improved bulk microphysics scheme. part ii: Implementation of a new snow parameterization, *Mon. Weather Rev.*, *136*, 5095–5115, doi:10.1175/2008MWR2387.1.

Tiedtke, M. (1989), A comprehensive mass flux scheme for cumulus parameterization in large-scale models, *Mon. Weather Rev.*, *117*, 1779–1800.

Trier, S. B., R. D. Sharman, and T. P. Lane (2012), Influences of moist convection on a cold-season outbreak of clear-air turbulence (CAT), *Mon. Weather Rev.*, *140*, 2477–2496, doi:10.1175/MWR-D-11-00353.1.

Wang, P. K. (2003), Moisture plumes above thunderstorm anvils and their contributions to cross-tropopause transport of water vapor in midlatitudes, *J. Geophys. Res.*, *108*(D6), 4194, doi:10.1029/2002JD002581.

Weisman, M. L., W. C. Skamarock, and J. B. Klemp (1997), The resolution dependence of explicitly modeled convective systems, *Mon. Weather Rev.*, *125*, 527–548.

World Meteorological Organization (1957), Meteorology—A three-dimensional science: Second session of the commission for aerology, *World Meteorol. Organ. Bull.*, *4*, 134–138.

Zhang, C., Y. Wang, and E. Hamilton (2011), Improved representation of boundary layer clouds over the southeast Pacific in ARW-WRF using a modified Tiedtke cumulus parameterization scheme, *Mon. Weather Rev.*, *139*, 3489–3513, doi:10.1175/MWR-D-10-05091.1.